Force-Force Correlations in Disordered Magnets

Cathelijne ter Burg[1], Felipe Bohn[2], Gianfranco Durin[3], Rubem Luis Sommer[4], Kay Jörg Wiese[1]
[1] *Laboratoire de Physique de l'École Normale Supérieure, ENS, Université PSL, CNRS, Sorbonne Université, Université Paris-Diderot, Sorbonne Paris Cité, 24 rue Lhomond, 75005 Paris, France*
[2] *Departamento de Física, Universidade Federal do Rio Grande do Norte, 59078-900 Natal, RN, Brazil*
[3] *Istituto Nazionale di Ricerca Metrologica, Torino, Italy*
[4] *Centro Brasileiro de Pesquisas Físicas, Rua Dr. Xavier Sigaud 150, Urca, 22290-180 Rio de Janeiro, RJ, Brazil*

We study experimentally the force-force correlator in Barkhausen noise, measured in different soft ferromagnets. Our materials belong to two distinct universality classes, differing in the range of spin interactions, and for both cases with and without eddy-current effects. We show that these correlations have a universal form predicted by the functional renormalization group, distinct for short-range and long-range elasticity, and mostly independent of eddy currents. For short-range elasticity, we find the correlator predicted in $d = 2$. For long-range elasticity we observe its 1-loop solution, relevant at the upper critical dimension. In all cases force-force correlations grow linearly at small distances, as is assumed in the ABBM model, but in contrast to the latter are bounded at large distances. As a consequence, avalanches are anti-correlated, i.e. reduced in size, at short distances. We derive bounds for these correlations, which are saturated in the experiments, showing that samples are chosen optimally and multiple magnetic domain walls effectively behave as a single wall.

Barkhausen noise in soft magnets [1–3] originates from complex microscopic magnetization processes through the jerky motion of magnetic domain walls. First discovered by H. Barkhausen [4] in 1919, it is the oldest example of depinning and avalanche motion [5–7]. Observables readily accessible are the avalanche size and duration [8, 9], as well as the avalanche shape [10–13]. On the theoretical side, mean-field models pioneered in 1990 by Alessandro, Beatrice, Bertotti and Montorsi (ABBM) [14, 15] have shaped our thinking. In these models, the domain wall is represented by a single degree of freedom, its centre of mass, a.k.a. *mean field* (MF). The question then arises how good this description is. A partial answer was given by experiments, which show the existence of two universality classes differing in the kind and range of interactions governing the domain-wall dynamics [6, 9]; they separate amorphous materials with short-range (SR) interactions from polycrystals with long-range (LR) interactions, the latter attributable to strong dipolar interactions. Another distinction is whether eddy currents (EC) play a noticeable effect for the wall motion [1, 6, 10, 11, 16], an aspect experimentally tunable by varying the sample thickness [1, 10, 11]. For the first class, key observables such as the avalanche-size exponent $\tau \simeq 1.27$ differ from their MF prediction $\tau_{\rm MF} = 3/2$, while they are correctly accounted for by field-theoretic models [17–19]. For LR magnets the experimentally observed exponents agree with their MF predictions, which led to the belief that MF theory is valid there.

In view of the solid evidence for critical exponents, a key question is whether an experiment can be designed which contradicts the ABBM model in one of its key predictions for LR magnets. We show below that this is indeed the case for the correlator of forces acting on the domain wall, or equivalently the correlator of its positions. In order to understand this, consider the equation of motion of an interface with SR interactions,

$$\eta \partial_t u(x,t) = \nabla^2 u(x,t) + m^2[w - u(x,t)] + F(x, u(x,t)), \qquad w = vt. \tag{1}$$

Here w is proportional to the external applied field, and we suppose that the latter increases very slowly. The term proportional to m^2, the *demagnetization factor*, is always present in magnetic systems, usually denoted $k \equiv m^2$ [6]. Under slow driving conditions, most of the time the l.h.s. of Eq. (1) vanishes. Averaging Eq. (1) over x, we arrive at[1]

$$\eta \dot{u}_w = m^2 [w - u_w] + F_w. \tag{2}$$

This is Newton's law: At rest, the forces exerted by the confining potential are balanced by the forces from the disorder. The key observable we study here are the interface correlations,

$$\hat{\Delta}_v(w - w') := \overline{[w - u_w][w' - u_{w'}]}^{\rm c} \simeq \frac{1}{m^4} \overline{F_w F_{w'}}^{\rm c}. \tag{3}$$

The index v reminds that $\hat{\Delta}_v$ depends on the driving velocity. The normalization is different from the one used in the field theory [20], which contains an additional factor of $m^4 L^d$, with L the system size, on the r.h.s. Our choice is motivated by a lack in the knowledge of m^2 and L, and by the reduction of scales in $\hat{\Delta}_v(w)$ to a single one, namely the correlation length ρ in w-direction. We are particularly interested in its zero-velocity limit

$$\hat{\Delta}(w) = \lim_{v \to 0} \hat{\Delta}_v(w). \tag{4}$$

The observable $\hat{\Delta}(w)$ is the central object of our work. It is also the central object of the field theory, necessary for all quantitative predictions [7, 20, 30–32]. In an experiment, it is impossible to take the limit of $v \to 0$. The effect of the finite driving velocity v is to round the cusp $|\hat{\Delta}'(0^+)| = \sigma$ (see Eq. (7)) in a boundary layer of size $\delta_w \sim v\tau$, where τ

[1] We denote by $u_w(x) := u(x,t)$ the interface position given $w = vt$, and

$$u_w := \frac{1}{L^d} \int_x u_w(x), \quad F_w := \frac{1}{L^d} \int_x F(x, u_w(x)).$$

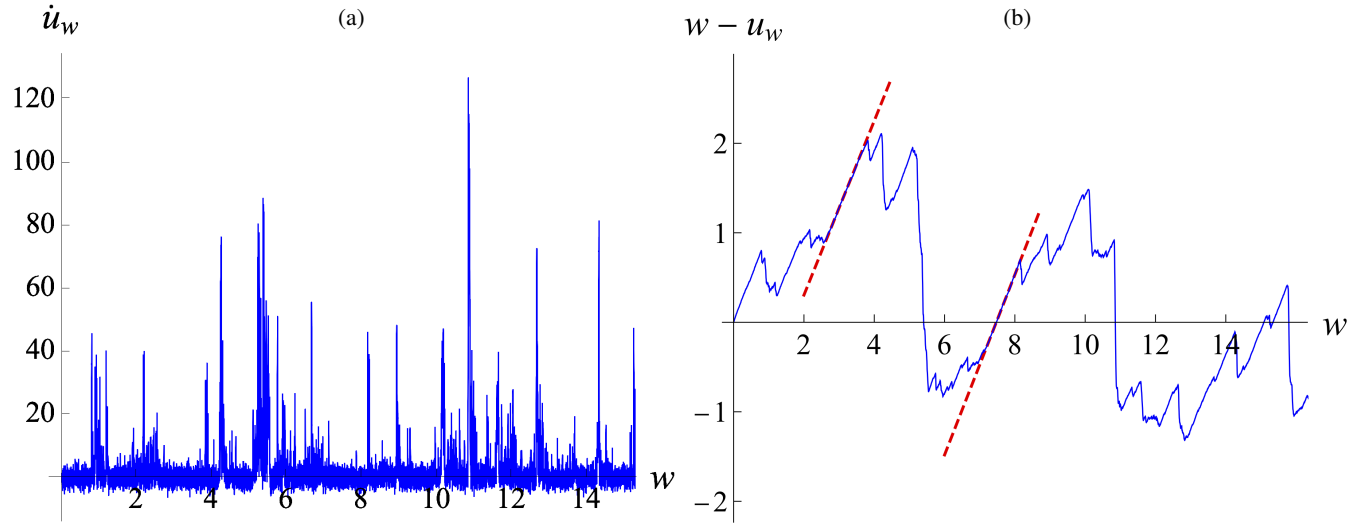

FIG. 1. Barkhausen noise in an amorphous FeSiB film with thickness of 200 nm, a bulk magnet with SR elasticity and without eddy-current effects. The signal in **(a)**, depicted in terms of $\dot{u}_w$ and w in our notation, is characterised by sudden bursts of activity which are recorded as a voltage signal in the pickup coil, due to changes in the magnetic flux. Background instrumental white noise is visible, leading to negative $\dot{u}_w$. **(b)** The connected part of the interface position, $w - u_w$, obtained after integration. The linearly increasing parts have slope one by construction, and correspond to an increasing magnetic field, followed by sudden jumps in force when the domain wall moves forward.

is the timescale set by the response function $R(t) \simeq \frac{1}{\tau}\mathrm{e}^{-t/\tau}$ (see Fig. 2(c) for an example). One can show [25] that

$$\hat{\Delta}_v(w) = \int_0^\infty \mathrm{d}t \int_0^\infty \mathrm{d}t' R(t)R(t')\hat{\Delta}(w - v(t-t')). \quad (5)$$

In Appendix D we summarize the method of Ref. [25] to *unfold* Eq. (5) and reconstruct $\hat{\Delta}(w)$ from the measured $\hat{\Delta}_v(w)$. The result is

$$\hat{\Delta}(w) = \hat{\Delta}_v(w) + \tau^2 \hat{\Delta}_{\dot{u}}(w), \quad (6)$$

where $\hat{\Delta}_{\dot{u}}(w)$ is the auto-correlation function of $\dot{u}_w$, readily accessible in our experiment. This allows us to extract the correlation function $\hat{\Delta}(w)$ in Eq. (4), by plotting the r.h.s. and finding the time scale τ that best eliminates the boundary layer. As we demonstrate below, Eq. (6) allows us to remove a relatively large boundary layer of size $\delta_w = v\tau$, but it creates a smaller one of size $\delta'_w = v\tau'$. This we believe is due to additional fast modes contributing to the response function in Eq. (5). This is further discussed in Appendix E.

In the small-v limit Eq. (5) can be approximated by a boundary-layer ansatz [25]. Whereas this method may be more robust for noisy data, it is less precise. We discuss this in Appendix D.

The ABBM model assumes the forces F_w to perform a random walk, and as a consequence[2]

$$\frac{1}{m^4}\frac{1}{2}\overline{[F_w - F_{w'}]^2} = \hat{\Delta}(0) - \hat{\Delta}(w - w') \simeq \sigma|w - w'|. \quad (7)$$

Field theory [7, 21, 22] predicts a combination $\hat{\Delta}(0) - \hat{\Delta}(w)$ which as Eq. (7) grows linearly for small w but saturates for large w. Its shape is distinct in SR and LR systems; analytical expressions are given in Appendix C.

The above framework has been tested in simulations [23–25], experiments on wetting [26], as well as RNA/DNA peeling [27]. Compared to these systems, magnets have important advantages: Firstly, they permit easy repetition, increasing the statistics; secondly, they are the only system where both LR and SR elasticity are realized.

Our measurement procedure is as follows: Eq. (3) above uses u_w, the position of the center of mass of the interface. Our experimental data consist of the Barkhausen-noise time series, itself proportional to the center-of-mass velocity $\dot{u}_w$. As can be seen in Fig. 1(a), this signal is characterized by bursts when the domain wall moves forward, and a vanishing signal when the wall is at rest, combined with background white noise from the measurement device[3]. This allows us to reconstruct u_w, as depicted in Fig. 1(b). The domain-wall position u_w is characterized by linearly increasing parts corresponding to an increasing magnetic field (i.e. w), followed by sudden drops in $w - u_w$ when the domain wall moves forward. Since the linear increase is due to w, its slope is one. This allows us to reconstruct the a priori unknown scale between $\dot{u}_w$ and the induced current, reducing the unknown scales in the experiment to a single one. Details of the construction of u_w from $\dot{u}_w$ are discussed in Appendix B.

We analyse $\hat{\Delta}(w)$ in different classes of materials, including polycrystals and amorphous materials. They are respec-

[2] Since F_w performs a random walk, $\overline{F_w}$ is not well defined, whereas Eq. (7) is.

[3] Since the interface only moves forward [28] $\dot{u}_w \geq 0$, incidences on Fig. 1 violating this condition are due to noise.

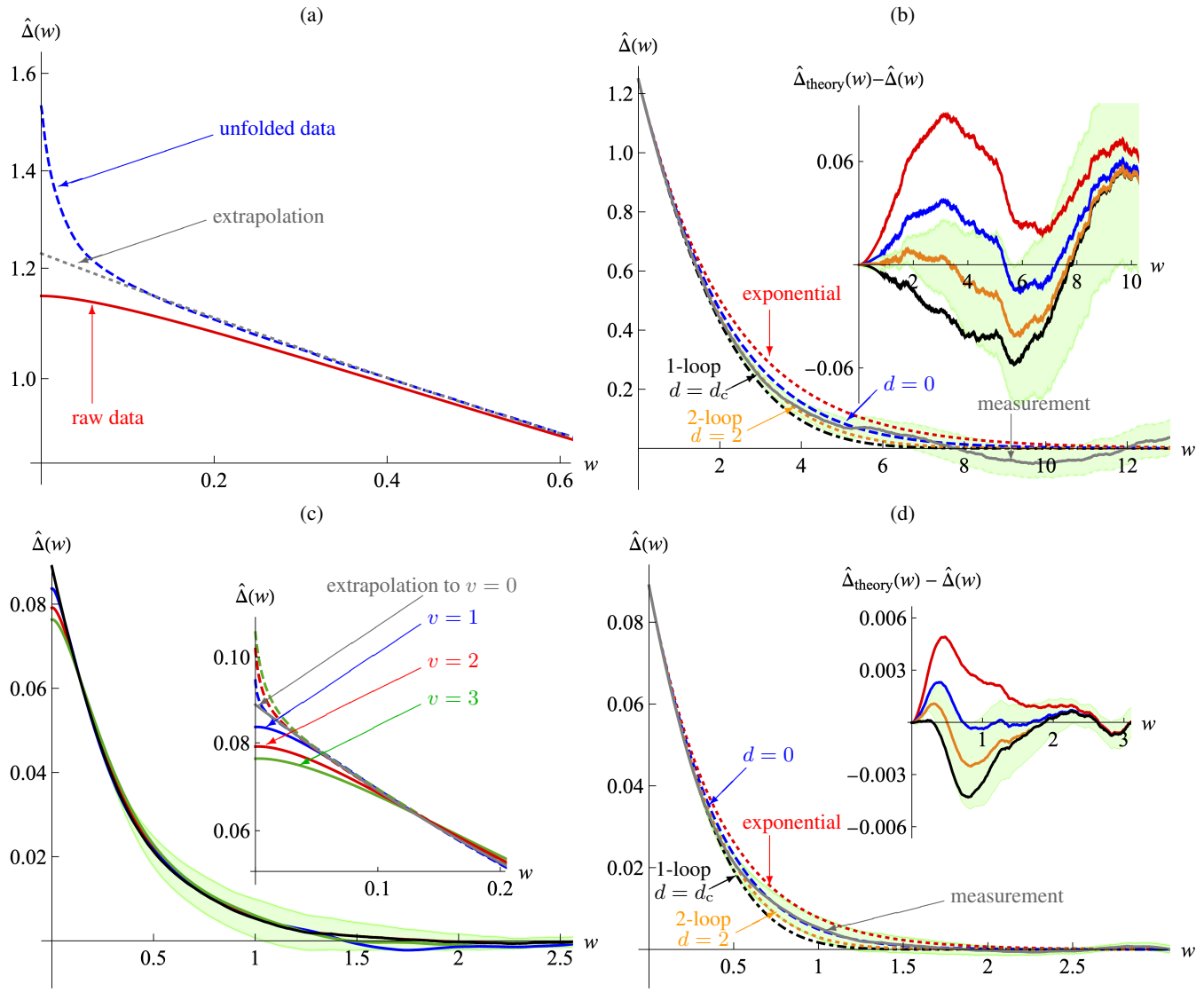

FIG. 2. **(a)** Construction of the fixed-point function $\hat\Delta(w)$ for the FeSiB film (SR elasticity, no eddy-current effects). In red the raw data. In blue dashed, the result from Eq. (6) using $\tau = 0.17$. In dotted gray the extrapolation to $w = 0$. The small remaining peak (blue dashed) is at a much smaller time scale. **(b)** Comparison of the fixed-point function using the dotted gray curve of (a), to theoretical candidates, fixing scales by $\hat\Delta(0)$ and $\hat\Delta'(0^+)$. The theory candidates from top to bottom are: exponential function (red, dotted), solution in $d = 0$ [25, 29] (blue, dashed), 2-loop FRG for $d = 2$ obtained by Pade resummation (orange, dotted), 1-loop FRG solution, valid for $d = d_c$ (black, dot-dashed). Error bars in green represent 1-σ confidence intervals. The inset shows theory minus data in the corresponding color code, favouring the $d = 2$ fixed point at two loops (with error bars for this curve only). **(c)** Check of the unfolding procedure, Eq. (6), for the FeCoB ribbon (SR elasticity, noticeable eddy currents), at different driving velocities v, using the same time scale $\tau = 0.025$; magnified in the inset. Apart from a small deviation for $v = 3$ they extrapolate to the same function. **(d)** Comparison of $\hat\Delta(w)$ from (c) to the theoretical candidates, using the same color code as in Fig. (b). The data is consistent with the 2-loop FRG fixed point at $\varepsilon = 2$.

tively characterized by long-range or short-range elasticity, both for thick and thin samples, i.e., with and without eddy currents. Table I summarises our set of samples and their properties. Details for the samples and experiments are given in Appendix A, and for the data analysis in Appendix F. There we also included the relevant information to convert our units of w to physical time and space.

Short-range interactions without eddy currents. Our first sample is an amorphous FeSiB film with a thickness of 200 nm. Fig. 2(a) shows that the raw data for $\hat\Delta(w)$ are rounded in a boundary layer of size $\delta_w \approx 0.6$, due to the finite driving velocity. To obtain the zero-driving-velocity limit $\hat\Delta(w)$, we use Eq. (6) with $\tau = 0.17$. This reduces the boundary layer (non-straight part) from $\delta_w \approx 0.6$ (in red, solid) to $\delta_w \approx 0.1$ (in blue, dashed), allowing us to extrapolate to $w = 0$ (shown in dotted grey). It is this curve we report as our final result on Fig. 2(b) (in solid grey).

The measured values for $\hat\Delta(0)$ and $\hat\Delta'(0^+)$ are then used to fix all scales in the fixed-point functions we wish to compare to on Fig. 2(b). These are from bottom to top (analytic ex-

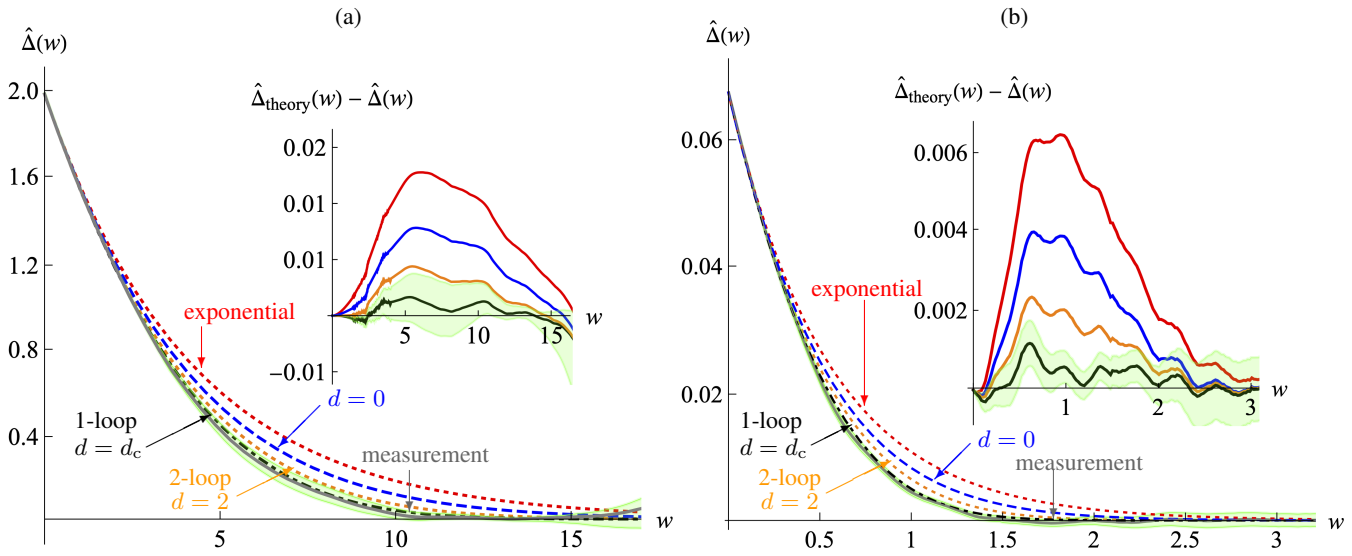

FIG. 3. The measured function $\hat{\Delta}(w)$ for our two LR samples, i.e., (a) a polycrystalline 200-nm-thick NiFe film (with negligible eddy-current effects), and (b) a polycrystalline FeSi ribbon (with eddy currents). Both measurements are in agreement with the 1-loop FRG fixed point.

pressions are given in Appendix C): 1-loop FRG (black, dot-dashed, relevant for $d = d_c$, i.e. LR elasticity), 2-loop FRG in $d = 2$ (relevant for SR elasticity, in orange, dotted) [21, 22], the $d = 0$ solution [25, 29] (blue, dashed) and a pure exponential (red, dotted), the latter, not realized in magnets, given as reference. The data agree best, and within error bars, with the 2-loop FRG fixed point predicted by the theory for $d = 2$. We note that from Fig. 2(b) we extract a correlation length $\rho := \hat{\Delta}(0)/\hat{\Delta}'(0) \approx 3$. This agrees with the scale on which $\hat{\Delta}_{\dot{u}}(w)$ decays to 0 (see Fig. 10(a) in Appendix G).

Short-range interactions with eddy currents. Our second sample with SR elasticity is an amorphous FeCoB ribbon where eddy currents are non-negligible. Here a range of different driving velocities is at our disposal. As eddy-current effects and non-linearities become more relevant as v increases, we focus on the small-v limit of $v = 1, 2, 3$. Whereas for the previous sample, finding $\hat{\Delta}_v(0)$ was sufficient, here there is additional (white) noise contributing to $\dot{u}$. After integration this contributes a linear function to $\hat{\Delta}(w)$, and what we measure is

$$\hat{\Delta}_v^{\text{raw}}(0) - \hat{\Delta}_v^{\text{raw}}(w) = \hat{\Delta}_v(0) - \hat{\Delta}_v(w) + \sigma_{\text{noise}}|w|, \quad (8)$$

necessitating to subtract a linear term $\sigma_{\text{noise}}|w|$ (see Fig. 8 in Appendix F 2). Fig. 2(c) shows $\hat{\Delta}_v(w)$ after this subtraction, for driving velocities $v = 1, 2, 3$ in blue, red and green. The inset shows a zoom into the boundary layer with unfolding by Eq. (6) in the same colour code. Having data at different v allows us to test that

(i) the boundary layer scales linearly in v, i.e. $\delta_w \sim v\tau$.

(ii) $\hat{\Delta}_v(w)$ for $v = 1, 2, 3$ unfold to the same $\hat{\Delta}(w)$.

Both conditions are satisfied using $\tau = 0.025$. Comparison to the fixed-point candidates proceeds as before and is shown in Fig. 2(d), using both $v = 1$ and $v = 2$ to improve the statistics. Although the error bars are non-negligible, the data is in agreement with the predicted 2-loop fixed point in $d = 2$, as for the FeSiB film with SR elasticity without eddy currents shown in Fig. 2(b). Note though that for $w > 0.7$ we observe a slower decay and the data slightly deviates from the 2-loop result, albeit well within error bars. We do not know whether this is a statistical fluctuation, or due to the eddy currents.

Long-range interactions without eddy currents. Long-range elasticity arises in materials, here a polycrystalline NiFe film with a thickness of 200 nm, due to strong dipolar interactions between parts of the magnetic domain wall. For long-range elasticity the upper critical dimension $d_c = 2$ coincides with the dimension of the domain wall. The common belief is that then MF theory, i.e. the ABBM model, is sufficient to describe the system. A glance at Fig. 3(a) shows that the experimental result is in contradiction to the prediction (7) of the ABBM model. While the latter holds at small w, at larger w the correlator $\hat{\Delta}(w)$ decays to zero. Field theory predicts

Sample	Interactions / Eddy currents	Correlation Length
Amorphous 200-nm-thick FeSiB film	SR / No	7.5 ms $\sim$ 495 μm
Amorphous FeCoB ribbon	SR / Yes	0.1 s $\sim$ 67.5 μm
Polycrystalline 200-nm-thick NiFe film	LR / No	12.5 ms $\sim$ 500 μm
Polycrystalline FeSi ribbon	LR / Yes	35 ms $\sim$ 0.9695 μm

TABLE I. The set of samples investigated in this work, belonging to two universality classes ascribed to the kind of interaction governing the domain-wall dynamics, i.e. short-range and long-range interactions. In addition, two of them are thin films with negligible eddy-current effects, while the other two are ribbons, known for the retarding effect of eddy currents. The correlation length ρ is given in physical units using the information in Appendix F.

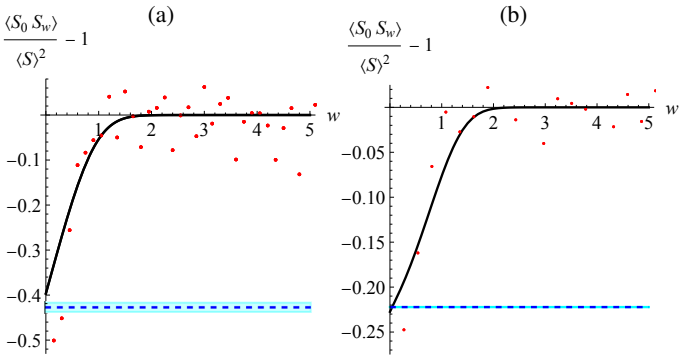

FIG. 4. Anticorrelation of avalanches as a function of w, for the two samples with eddy-current effects, (a) the FeCoB with SR elasticity and (b) the FeSi one with LR elasticity. The solid line is the prediction $-\hat{\Delta}''(w)$ from Eq. (9), as obtained from the experiment. The dashed lines are bounds on the maximally achievable reduction from the ε-expansion (10), with error bars in cyan, for the SR elasticity case. There are no fitting parameters.

[21, 22, 33, 34] that fluctuations are relevant at the upper critical dimension, and that the correlator $\hat{\Delta}(w)$ is given by the 1-loop FRG fixed point. Fig. 3(a) shows that this is indeed the case.

Long-range interactions with eddy currents. Our fourth sample is a polycrystalline FeSi ribbon where the elasticity is long-range and eddy currents non-negligible. Fig. 3(b) shows a comparison of the unfolded data to the four theoretical candidates. As for the NiFe film with LR elasticity without eddy-current effects, the agreement is excellent with the 1-loop FRG solution, and inconsistent with ABBM. We refer to Appendix F 4 and Fig. 9 for details on the data analysis for this sample.

Curiously, the question of the effective force-force or center-of-mass correlations, the correlations of velocities or avalanche sizes have never been addressed experimentally. Here we aim at closing this gap. We show that these correlations have a universal form, predicted by the functional renormalization group [7, 20–22, 31, 32], both for short-range and long-range elasticity and mostly independent of eddy currents.

An important property of the experiments is that force-force correlations are always bounded, and do not grow indefinitely as in mean-field models such as the ABBM model [14, 15], see Eq. (7). It has been shown (see Ref. [7], section 4.20, or Eq. (8) of Ref. [35]) that as a consequence, avalanches are anti-correlated

$$\frac{\langle S_{w_1} S_{w_2}\rangle}{\langle S\rangle^2} - 1 = -\hat{\Delta}''(w_1 - w_2). \tag{9}$$

Here S_w is the size of an avalanche at w, and by definition $\langle S_w\rangle = \langle S\rangle$. In the numerator is $\langle S_{w_1} S_{w_2}\rangle$, the expectation of the product of avalanche sizes, given that one was triggered at $w = w_1$, and a second at $w = w_2$. The experimental verification of this relation is shown on Fig. 4. Despite large statistical fluctuations, both the functional form as the amplitude agree. Since $\hat{\Delta}(w)$ is convex, $\hat{\Delta}''(w) \geq 0$. On the other hand, $\langle S_{w_1} S_{w_2}\rangle \geq 0$, thus $\hat{\Delta}''(w) \leq 1$. This bound is impossible to reach, as the toy-model (C6) in dimension $d = 0$ has $\hat{\Delta}''(0^+) = 0.5$. The ε-expansion [7] gives

$$\hat{\Delta}''(0^+) \leq \frac{2}{9} + 0.107533\varepsilon + \mathcal{O}(\varepsilon^2), \tag{10}$$

which evaluates to 0.437 for SR, and 0.222 for LR correlations. A glance at Fig. 4 shows that this bound is saturated, both for the SR and LR sample. This is surprising as both systems have multiple domain walls, estimated to be around five for the samples on Fig. 4. So either all but one domain wall are completely stuck, or these multiple walls are so highly correlated that they effectively behave as a single wall.

We hope this work inspires the experimental community to look beyond the commonly studied observables and beyond mean field. Further experimental systems which are interesting to explore are sheered colloids or foams, DNA unzipping, and earthquakes.

ACKNOWLEDGMENTS

We thank A. Douin, F. Lechenault, G. Mukerjee and A. Rosso for discussions. F.B. and R.L.S. acknowledge financial support from the Brazilian agencies CNPq and CAPES.

[1] F. Bohn, G. Durin, M. A. Correa, N. R. Machado, R. D. Della Pace, C. Chesman, R. L. Sommer, *Playing with universality classes of Barkhausen avalanches*, Sci. Rep. **8** (2018) 11294.

[2] F. Bohn, M. A. Corrêa, M. Carara, S. Papanikolaou, G. Durin and R. L. Sommer, *Statistical properties of Barkhausen noise in amorphous ferromagnetic films*, Phys. Rev. E **90** (2014) 032821.

[3] F. Bohn, M.A. Corrêa, A. Da Cas Viegas, S. Papanikolaou, G. Durin and R. L. Sommer, *Universal properties of magnetization dynamics in polycrystalline ferromagnetic films*, Phys. Rev. E **88** (2013) 032811.

[4] H. Barkhausen, *Zwei mit Hilfe der neuen Verstärker entdeckte Erscheinungen*, Phys. Ztschr. **20** (1919) 401–403.

[5] J.P. Sethna, K.A. Dahmen and C.R. Myers, *Crackling noise*, Nature **410** (2001) 242–250.

[6] G. Durin and S. Zapperi, *The Barkhausen effect*, in G. Bertotti and I. Mayergoyz, editors, *The Science of Hysteresis*, page 51, Amsterdam, 2006, cond-mat/0404512.

[7] K.J. Wiese, *Theory and experiments for disordered elastic manifolds, depinning, avalanches, and sandpiles*, (2021), arXiv:2102.01215.

[8] O. Perkovic, K. Dahmen and J.P. Sethna, *Avalanches, Barkhausen noise, and plain old criticality*, Phys. Rev. Lett.

75 (1995) 4528–4531.
[9] G. Durin and S. Zapperi, *Scaling exponents for Barkhausen avalanches in polycrystalline and amorphous ferromagnets*, Phys. Rev. Lett. **84** (2000) 4705–4708.
[10] S. Zapperi, C. Castellano, F. Colaiori, G. Durin, *Signature of effective mass in crackling-noise asymmetry* Nat. Phys. **1** (2005) 46–49.
[11] S. Papanikolaou, F. Bohn, R.L. Sommer, G. Durin, S. Zapperi and J.P. Sethna, *Universality beyond power laws and the average avalanche shape*, Nature Physics **7** (2011) 316–320.
[12] L. Laurson, X. Illa, S. Santucci, K.T. Tallakstad, K.J. Måløy and M.J. Alava, *Evolution of the average avalanche shape with the universality class*, Nat. Commun. **4** (2013) 2927.
[13] G. Durin, F. Bohn, M.A. Correa, R.L. Sommer, P. Le Doussal and K.J. Wiese, *Quantitative scaling of magnetic avalanches*, Phys. Rev. Lett. **117** (2016) 087201, arXiv:1601.01331.
[14] B. Alessandro, C. Beatrice, G. Bertotti and A. Montorsi, *Domain-wall dynamics and Barkhausen effect in metallic ferromagnetic materials. I. Theory*, J. Appl. Phys. **68** (1990) 2901.
[15] B. Alessandro, C. Beatrice, G. Bertotti and A. Montorsi, *Domain-wall dynamics and Barkhausen effect in metallic ferromagnetic materials. II. Experiments*, J. Appl. Phys. **68** (1990) 2908.
[16] A. Dobrinevski, P. Le Doussal and K.J. Wiese, *Non-stationary dynamics of the Alessandro-Beatrice-Bertotti-Montorsi model*, Phys. Rev. E **85** (2012) 031105, arXiv:1112.6307.
[17] D.S. Fisher, *Collective transport in random media: From superconductors to earthquakes*, Phys. Rep. **301** (1998) 113–150.
[18] A. Dobrinevski, P. Le Doussal and K.J. Wiese, *Avalanche shape and exponents beyond mean-field theory*, EPL **108** (2014) 66002, arXiv:1407.7353.
[19] A. Dobrinevski, *Field theory of disordered systems – avalanches of an elastic interface in a random medium*, PhD Thesis, ENS Paris (2013), arXiv:1312.7156.
[20] P. Le Doussal and K.J. Wiese, *How to measure Functional RG fixed-point functions for dynamics and at depinning*, EPL **77** (2007) 66001, cond-mat/0610525.
[21] P. Chauve, P. Le Doussal and K.J. Wiese, *Renormalization of pinned elastic systems: How does it work beyond one loop?*, Phys. Rev. Lett. **86** (2001) 1785–1788, cond-mat/0006056.
[22] P. Le Doussal, K.J. Wiese and P. Chauve, *2-loop functional renormalization group analysis of the depinning transition*, Phys. Rev. B **66** (2002) 174201, cond-mat/0205108.
[23] A.A. Middleton, P. Le Doussal and K.J. Wiese, *Measuring functional renormalization group fixed-point functions for pinned manifolds*, Phys. Rev. Lett. **98** (2007) 155701, cond-mat/0606160.
[24] A. Rosso, P. Le Doussal and K.J. Wiese, *Numerical calculation of the functional renormalization group fixed-point functions at the depinning transition*, Phys. Rev. B **75** (2007) 220201, cond-mat/0610821.
[25] C. ter Burg and K.J. Wiese, *Mean-field theories for depinning and their experimental signatures*, Phys. Rev. E **103** (2021) 052114, arXiv:2010.16372.
[26] P. Le Doussal, K.J. Wiese, S. Moulinet and E. Rolley, *Height fluctuations of a contact line: A direct measurement of the renormalized disorder correlator*, EPL **87** (2009) 56001, arXiv:0904.4156.
[27] K.J. Wiese, M. Bercy, L. Melkonyan and T. Bizebard, *Universal force correlations in an RNA-DNA unzipping experiment*, Phys. Rev. Research **2** (2020) 043385, arXiv:1909.01319.
[28] A.A. Middleton, *Asymptotic uniqueness of the sliding state for charge-density waves*, Phys. Rev. Lett. **68** (1992) 670–673.
[29] P. Le Doussal and K.J. Wiese, *Driven particle in a random landscape: disorder correlator, avalanche distribution and extreme value statistics of records*, Phys. Rev. E **79** (2009) 051105, arXiv:0808.3217.
[30] T. Nattermann, S. Stepanow, L.-H. Tang and H. Leschhorn, *Dynamics of interface depinning in a disordered medium*, J. Phys. II (France) **2** (1992) 1483–8.
[31] O. Narayan and D.S. Fisher, *Threshold critical dynamics of driven interfaces in random media*, Phys. Rev. B **48** (1993) 7030–42.
[32] P. Le Doussal, *Finite temperature Functional RG, droplets and decaying Burgers turbulence*, Europhys. Lett. **76** (2006) 457–463, cond-mat/0605490.
[33] A. Fedorenko and S. Stepanow, *Depinning transition at the upper critical dimension*, Phys. Rev. E **67** (2003) 057104, cond-mat/0209171.
[34] P. Le Doussal and K.J. Wiese, *Higher correlations, universal distributions and finite size scaling in the field theory of depinning*, Phys. Rev. E **68** (2003) 046118, cond-mat/0301465.
[35] T. Thiery, P. Le Doussal and K.J. Wiese, *Universal correlations between shocks in the ground state of elastic interfaces in disordered media*, Phys. Rev. E **94** (2016) 012110, arXiv:1604.05556.
[36] E. F. Silva, M. A. Correa, R. D. Della Pace, C. C. Plá Cid, P. R. Kern, M. Carara, C. Chesman, O. Alves Santos, R. L. Rodríguez-Suárez, A. Azevedo, S. M. Rezende, F. Bohn, *Thickness dependence of the magnetic anisotropy and dynamic magnetic response of ferromagnetic NiFe films*, J. Phys. D. Appl. Phys. **50** (2017) 185001.

Appendix: Supplementary Material

Appendix A: Samples and experiments

In this work, we analyze force-force correlations in soft magnetic materials. We employ two thin films and two ribbons to perform our Barkhausen-noise experiments. The thin films consist of an amorphous $Fe_{75}Si_{15}B_{10}$ (FeSiB) film and a polycrystalline $Ni_{81}Fe_{19}$ (NiFe) film, both with a thickness of 200 nm. The films are prepared by magnetron sputtering onto glass substrates, with dimensions 10 mm $\times$ 4 mm, using the parameters given in Refs. [2, 3]. Detailed information on the structural and magnetic characterizations is provided in Refs. [1–3, 11, 36]. Our ribbons are an amorphous $Fe_{64}Co_{21}B_{15}$ (FeCoB) and a polycrystalline FeSi alloy with Si=7.8%. Both ribbons have dimensions of about 20 cm $\times$1 cm, with thickness of $\sim 20\,\mu$m. Further information on the ribbons and their magnetic behavior are given in Refs. [6, 9].

Regarding the Barkhausen experiments, we record noise time series using the traditional inductive technique in an open magnetic circuit, in which one detects voltage pulses with a pickup coil wound around a ferromagnetic material submitted to a smooth, slow-varying external magnetic field. In our setup, sample and pickup coils are inserted in a long solenoid with compensation for the borders to ensure an homogeneous applied magnetic field on the sample. The sample is driven by a triangular magnetic field, applied along the main axis of the sample, with an amplitude high enough to saturate it mag-

netically. The pickup coil is wound around the central part of the sample. A second pickup coil, with the same cross section and number of turns, is used to compensate the signal induced by the magnetizing field. The Barkhausen signal is then amplified, filtered, and finally digitalized.

For the thin films, the Barkhausen experiments are performed in Brazil. The measurements are carried out using a pickup coil with 400 turns, 3.5 mm long and 4.5 mm wide, and under similar conditions, i.e., 50 mHz triangular magnetic field, 100 kHz 12-dB/octave low-pass filter set in the preamplifier (SR560 Stanford Research Systems) and signal acquisition taken with an analog-to-digital converter board (PCI-DAS4020/12 Measurement Computing) with sampling rate of 4×10^6 samples per second [1]. At a preanalysis stage, we employ a Wiener deconvolution [11], which optimally filters the background noise and removes distortions introduced by the response functions of the measurement apparatus in the original voltage pulses, thus providing reliable statistics despite the reduced intensity of the signal.

For the ribbons, the experiments are performed in Italy. They are carried out using a pickup coil with 50 turns, 1 mm long and 1 cm wide, a triangular magnetic field with frequency between 3-50 mHz, and a low-pass preamplifier filter chosen in the 3-20 kHz range, roughly half of the sampling rate. Specifically, we consider sampling rate of 50×10^3 samples per second for FeCoB, and 20×10^3 samples per second for FeSi [6, 9]. For the FeCoB ribbon, the sample is submitted to a small tensile stress of 2 MPa during the measurement in order to enhance the signal-to-noise ratio.

All time series for films and ribbons are acquired around the central part of the hysteresis loop, near the coercive field, where the domain wall motion is the main magnetization mechanism and the noise achieves the condition of stationarity [6]. For each experimental run, the statistical properties are obtained from at least 150 measured time series.

While the central issue in this work is to explore the force-force correlations from the Barkhausen-noise time series, the classification into the different universality classes reposes on earlier work, where we identified the universality class of Barkhausen avalanches by measuring the distributions of avalanche sizes and durations, the average size as a function of the avalanche duration, their power spectrum, and the average avalanche shape. The results for the thin films can be found in Refs. [1–3, 11], the ones for the ribbons in Refs. [6, 9].

Appendix B: Subtraction of the baseline and measurement of $\hat{\Delta}(w)$

Here we present the methods used to obtain the correlator $\hat{\Delta}_v(w)$ defined in Eq. (3) from the experimental data for the change in flux $\dot{u}_{w=vt} \equiv \dot{u}(t)$. As the magnetic field is increased at a rate v

$$u_w - w = \int_0^{w/v} \mathrm{d}t\, [\dot{u}^{\mathrm{raw}}(t) - v]. \tag{B1}$$

We found that there are strong sample-to-sample fluctuations for the mean $v_i := \langle \dot{u}_{\mathrm{raw}} \rangle_i$ in sample i, due to a drift in the amplifier baseline. If the estimate for v in (B1) is not correct, this adds a term of the form cw to $u_w - w$, with c a random number. If we suppose that c is Gauss-distributed with mean 0, integration leads to a parabolic contribution, i.e. $\hat{\Delta}_v(w) \to \hat{\Delta}_v(w) + \frac{1}{2}\langle c^2 \rangle w^2$. To correct this, we proceed as follows: For each sample i we consider the distribution $P(\dot{u})$ (see Fig. 5), and fit a Gaussian to its peak. This is done by choosing the data points which satisfy $P(\dot{u}) > 0.25 \max_{\dot{u}} P(\dot{u})$, and then fitting a parabola to $\ln[P(\dot{u})]$. Finally, $\dot{u}$ is shifted so that the maximum of the parabola lies at $\dot{u} = 0$. Our best estimate for the driving velocity is then the sample average over N runs,

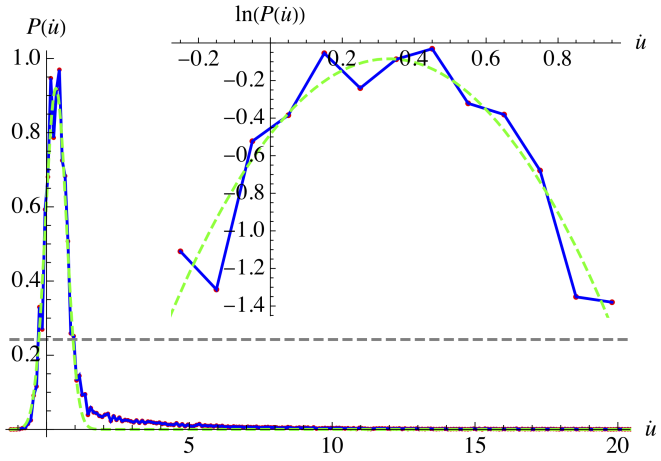

FIG. 5. Distribution $P(\dot{u})$ (blue, solid) with fit (green, dashed) to all data points above the dashed line. It is obtained from the optimal parabolic fit for $\ln P(\dot{u})$, as shown in the inset. The $\dot{u}$-value at the maximum of the fit is used as the position for the zero of $\dot{u}$.

$$v = \frac{1}{N} \sum_{i=1}^{N} \langle \dot{u} \rangle_i. \tag{B2}$$

This allows us to construct the interface position $u_w - w$ for sample i as

$$u_w^i - w = \int_0^{w/v} \mathrm{d}t\, [\dot{u}_i(t) - v]. \tag{B3}$$

The experimental setup makes appear an additional numerical prefactor on the r.h.s. of Eq. (B3). It is eliminated by demanding that the linearly increasing parts of Fig. 1 have slope 1.

The interface positions' connected two-point correlations are

$$\mathcal{M}_i(w - w') := \frac{1}{2} \left\langle \left[(u_w - w) - (u_{w'} - w') \right]^2 \right\rangle_i. \tag{B4}$$

Whereas the $\mathcal{M}_i$ show strong fluctuations (see Fig. 6), their mean (black)

$$\hat{\Delta}_v(0) - \hat{\Delta}_v(w) = \frac{1}{N} \sum_{i=1}^{N} \mathcal{M}_i(w) \tag{B5}$$

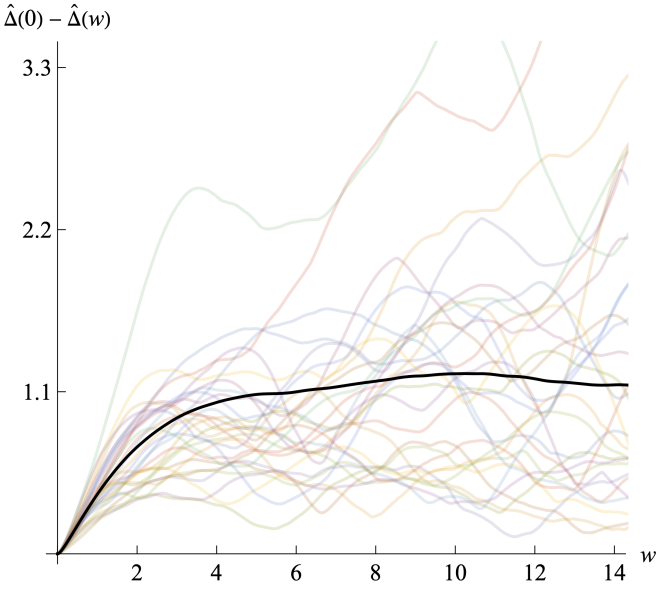

FIG. 6. The correlator $\hat{\Delta}_v(w)$ as given by Eq. (B5) for the FeSiB film (black) with SR elasticity and no eddy-current effects. Shaded in the background are the averages $\mathcal{M}_i$ over a single sweep from (B4) which show strong sample-to-sample fluctuations.

is more stable. $\hat{\Delta}_v(0)$ is extracted from the plateau value at large w (see Fig. 6). Statistically, the small-w region is more robust than the large-w tail. Due to the large fluctuations between the samples $\mathcal{M}_i$, error bars are computed using a statistical resampling method. One randomly divides all datasets into two parts and computes the variance of the partial means. Averaging this over 100 random partitions gives a robust estimate for the variance (see [27] for details). To obtain the error bars for the shape shown in the main text, all partial means have been rescaled such that their derivative at $w = 0$ equals the mean of $\hat{\Delta}'(0^+)$ over all samples. This takes out amplitude fluctuations and reduces the error bars to errors of the shape.

Appendix C: Theory predictions for the different classes

The extracted fixed-point function $\hat{\Delta}(w)$ can be compared to several theoretical candidates given below: the 1-loop FRG fixed point in Eq. (C4), the 2-loop FRG fixed point in $d = 2$ obtained by Pade resummation, optimized to agree with Eq. (C6) in $d = 0$, the solution (C6) in $d = 0$, and an exponential function. Each function contains two scales, the amplitude $\hat{\Delta}(0)$ and a correlation length in w-direction

$$\rho := \frac{\hat{\Delta}(0)}{|\hat{\Delta}'(0^+)|}. \tag{C1}$$

Rescaling the theory candidates to have the same $\hat{\Delta}(0)$ and $\Delta'(0^+)$ ensures that one compares the shape without any fitting parameter.

The dimension-dependent theoretical predictions rely on

$\hat{\Delta}(w)$	$\frac{\hat{\Delta}(0)\hat{\Delta}''(0)}{\hat{\Delta}'(0^+)^2}$	$\hat{\Delta}''(0)$
Exponential	1	1
$d = 0$, Eq. (C6)	0.822	$\frac{1}{2}$
2-loop FRG for $d = 2$ (SR)	0.75	≤ 0.437
1-loop FRG, Eq. (C3) (LR)	$\frac{2}{3}$	$\leq \frac{2}{9}$
SR elasticity without ECs	0.73(3)	0.37(2)
SR elasticity with ECs	0.65(10)	0.41(2)
LR elasticity without ECs	0.58(10)	0.17(5)
LR elasticity with ECs	0.65(10)	0.24(4)

TABLE II. Comparison of theoretically and experimentally obtained amplitudes and amplitude ratios.

the functional renormalization group (FRG). Contrary to conventional RG, where one considers the flow of a single coupling constant, the FRG follows the flow of an entire function. Writing $\varepsilon = d_c - d$ for the expansion parameter around the upper critical dimension d_c, the FRG fixed-point equation at 1-loop order reads

$$\begin{aligned}\partial_l \tilde{\Delta}(w) \; =& (\varepsilon - 2\zeta)\tilde{\Delta}(w) + \zeta u \tilde{\Delta}'(w) \\ & - \frac{\mathrm{d}^2}{\mathrm{d}w^2}\frac{1}{2}\big[\tilde{\Delta}(w) - \tilde{\Delta}(0)\big]^2 + \dots \end{aligned} \tag{C2}$$

with the dots representing higher-order contributions [21, 22] in an expansion in ε. The 1-loop solution to the fixed-point equation $\partial_\ell \tilde{\Delta}(w) = 0$ associated to Eq. (C2) is (see e.g. Ref. [7])

$$\tilde{\Delta}(w) = -\frac{\varepsilon}{3} W\left(-\exp\left(-\frac{w^2}{2} - 1\right)\right) + \mathcal{O}(\varepsilon^2). \tag{C3}$$

Here $W(z)$ is the product-log function, the principle solution for x in $z = xe^x$. The observable in Eq. (3) is obtained from the (scale-free) fixed-point solution $\tilde{\Delta}(w)$ as

$$\hat{\Delta}(w) \; = \; \mathcal{A}\hat{\rho}^2 \tilde{\Delta}(w/\hat{\rho}), \tag{C4}$$

$$\hat{\rho} := \rho \frac{|\tilde{\Delta}'(0)|}{\tilde{\Delta}(0)}. \tag{C5}$$

The amplitude $\mathcal{A}$ is a number (depending on mL), whereas the correlation length ρ of Eqs. (C1) and (C4) scales as $\rho \sim m^{-\zeta}$. The fixed point (C3) gets corrected at 2-loop order [21, 22]. In principle, it allows us to predict $\hat{\Delta}(w)$ for domain-wall dimensions between $d = 4$ down to $d = 0$. The bulk magnets used here have $d = 2$ ($\varepsilon = 2$), whereas a thin magnetic film has $d = 1$ ($\varepsilon = 3$). Dimension $d = 0$ ($\varepsilon = 4$) is realized in the DNA/RNA peeling experiment of Ref. [27]. The precision of the approximation decreases with d, since the expansion parameter $\varepsilon = 4-d$ increases. We are in the fortunate position to have an analytic solution in $d = 0$ [25, 29],

$$\tilde{\Delta}(w) = \frac{w^2}{2} + \mathrm{Li}_2(1 - \mathrm{e}^w) + \frac{\pi^2}{6}. \tag{C6}$$

This allows us to choose a Padé approximant optimized for agreement with the exact solution (C6). A summary of the predictions for the different classes is presented in Tab. II.

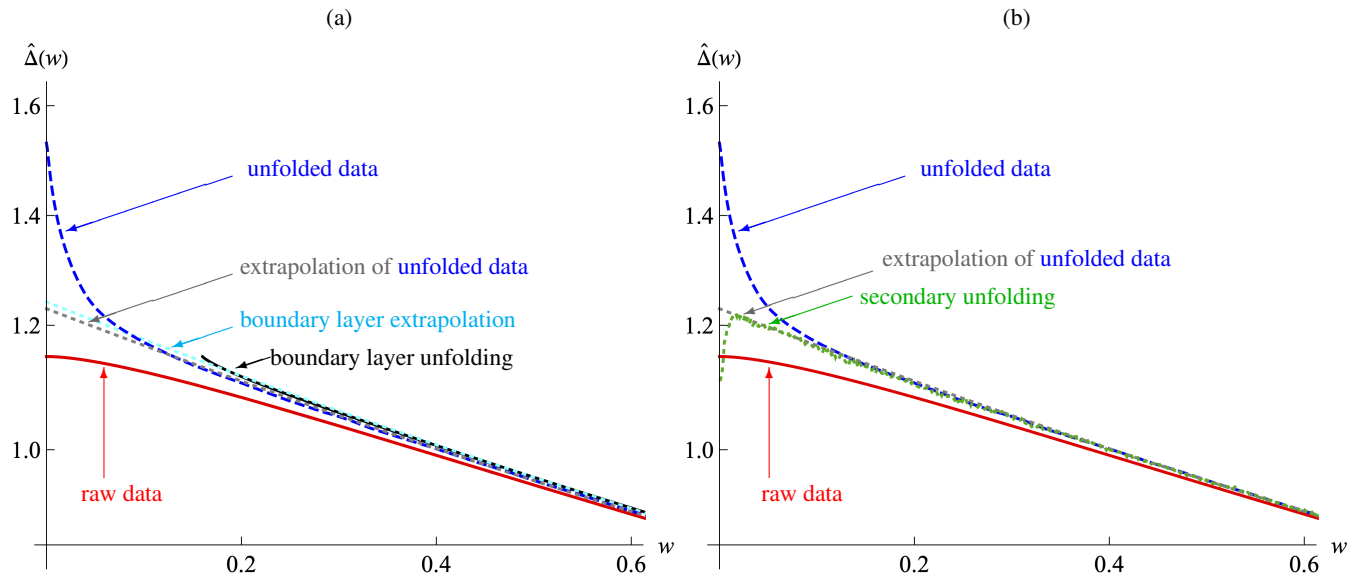

FIG. 7. Comparison of three different unfolding procedure for the 200-nm-thick FeSiB film with SR elasticity and no eddy currents (raw data in solid, red): unfolding via Eq. (D7) as discussed in the main text (blue dashed), time scale $\tau = 0.175$, and extrapolation (grey, dotted). In (a) is shown in addition unfolding via the boundary layer given by Eqs. (D7)-(D8) (black, solid) using the same $\tau = 0.175$, and its extrapolation (cyan, dotted). In (b) is shown the result of secondary unfolding using Eq. (E1) (green, dotted), with $\tau = 0.175$ and $\tau' = 0.0024$.

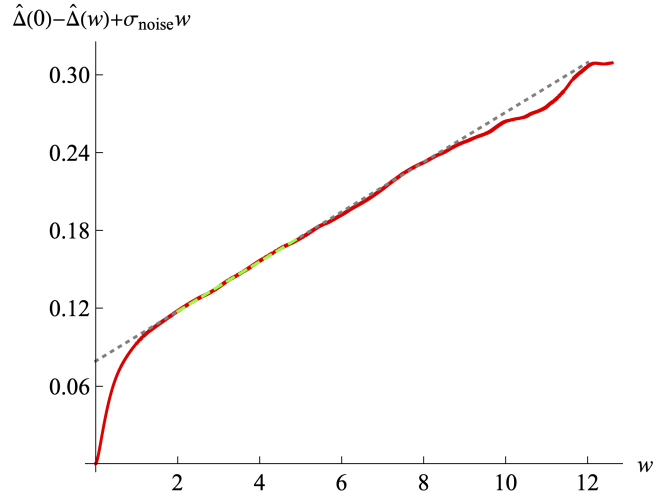

FIG. 8. Subtraction of a linear noise contribution (grey dotted, fitting region in green dashed) $\Delta(0) + \sigma_{\rm noise}|w|$ for the FeCoB ribbon with SR elasticity and eddy currents at $v = 2$.

Appendix D: Unfolding of $\hat{\Delta}_v(w)$.

Suppose the response function decays exponentially with time scale τ,

$$R(t) = \frac{1}{\tau} e^{-t/\tau}\Theta(t). \tag{D1}$$

Then it satisfies the differential equation

$$(1 + \tau\partial_t)R(t) = \delta(t), \tag{D2}$$

and is normalized,

$$\int_0^\infty R(t)\mathrm{d}t = 1. \tag{D3}$$

This allows us to invert Eq. (5) as [25]

$$\begin{aligned}\hat{\Delta}(w) &= (1 + v\tau\partial_w)(1 - v\tau\partial_w)\hat{\Delta}_v(w)\\ &= (1 - (v\tau)^2\partial_w^2)\hat{\Delta}_v(w).\end{aligned} \tag{D4}$$

Taking derivatives of the measured function $\hat{\Delta}_v(w)$ is noisy, but we are in the fortunate position to have direct access to the velocity correlation function $\hat{\Delta}_{\dot{u}}(w)$,

$$\hat{\Delta}_{\dot{u}}(w - w') := \overline{\dot{u}_w \dot{u}_{w'}} = -v^2\hat{\Delta}_v''(w - w'). \tag{D5}$$

Using this in Eq. (D4) we get Eq. (6) of the main text,

$$\hat{\Delta}(w) = \hat{\Delta}_v(w) + \tau^2\hat{\Delta}_{\dot{u}}(w). \tag{D6}$$

In the small-v limit Eq. (5) can be approximated by a boundary-layer ansatz [7, 25], which gives an alternative, robust, albeit less precise, unfolding procedure,

$$\hat{\Delta}_v(w) = \hat{\Delta}(\tilde{w}), \tag{D7}$$

$$\tilde{w} := \sqrt{w^2 + (v\tau)^2}. \tag{D8}$$

Our second strategy to reconstruct $\hat{\Delta}(w)$ is to plot $\hat{\Delta}_v(w)$ *vs.* $\tilde{w}$, and determine τ which gives the straightest curve at small $\tilde{w}$. An example is shown in Fig. 7(a).

Appendix E: Higher-order unfolding

We showed that application of Eq. (D6) to the measured $\hat{\Delta}_v(w)$ removes part of the boundary layer $\delta_w = v\tau$, but that

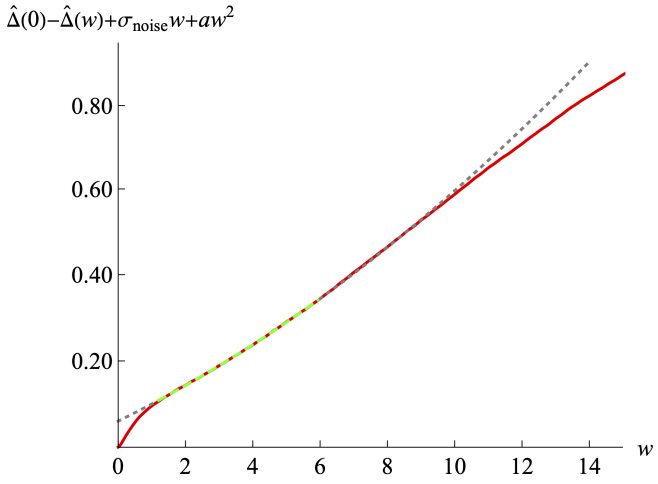

FIG. 9. Subtraction of the noise contribution $\hat{\Delta}(0) + \sigma_{\rm noise}|w| + aw^2$ with a small parabolic contribution (grey dotted, fitting region in green dashed) for the FeSi ribbon with LR elasticity and eddy currents at $v = 1$. The parabolic term with $a \geq 0$ results from small errors in the procedure of Appendix B to estimate the baseline of $\dot{u}_w$.

it creates a new smaller boundary layer of size δ'_w. On a phenomenological level, we found that inclusion of an additional term substantially improves the accuracy,

$$\hat{\Delta}(w) = \hat{\Delta}_v(w) + \tau^2\Big[1 + v\tau'\partial_w + ...\Big]\hat{\Delta}_{\dot{u}}(w). \quad \text{(E1)}$$

Such a term may arise for a non-exponentially decaying response function $R(t)$. In principle, the procedure can be improved using a second-order derivative in the square brackets. While a single derivative of $\hat{\Delta}_{\dot{u}}(w)$ still gives a signal relatively free of noise, adding a second derivative is not possible for our data. In Fig. 7(b) we show for the FeSiB film the result of the unfolding (D6) compared to the improved unfolding (E1).

Appendix F: Details for the four samples

1. FeSiB film: SR interactions without eddy currents

For the amorphous FeSiB film with thickness of 200 nm, we show in Fig. 6 the means $\mathcal{M}_i$ for a single run (in color), compared to the mean $N^{-1}\sum_{i=1}^{N}\mathcal{M}_i$ over all N runs (in black). $\hat{\Delta}_v(0)$ is extracted from the plateau value at large w. Subtracting $\hat{\Delta}_v(0)$ gives the curve reported in the main text in Fig. 2. In Fig. 7 we show for the same sample comparison of unfolding via Eq. (6) discussed in the main text, unfolding via the boundary layer (D7)-(D8) and secondary unfolding via Eq. (E1). All procedures are in quantitative agreement. In our chosen units, $w = 1$ corresponds to 2.5 ms, assuming a single wall to estimate the driving velocity. Due to the high level of correlation between the walls, we believe this estimation is justified. The number of domain walls is estimated to be around 3000 [1].

2. FeCoB ribbon: SR interactions with ECs

For the amorphous FeCoB ribbon, Fig. 8 shows the subtraction of $\hat{\Delta}(0)$ plus an additional linear contribution due to white noise as given in Eq. (8). All data presented in the main text are after this subtraction. In our chosen units, $w = 1$ corresponds to 0.2 s $\sim$ 135 μm. The number of domain walls is estimated be around 5.

3. NiFe film: LR interactions without ECs

Unfolding as presented in Fig. 3(a) for the polycrystalline NiFe film having thickness of 200 nm is done using $\tau = 0.39$. In our chosen units, $w = 1$ corresponds to 2.5 ms $\sim$ 100 μm. The number of domain walls is estimated to be around 5000 [36].

4. FeSi ribbon: LR interactions with ECs

Fig. 9 shows the subtraction of a linear term plus a small parabolic contribution for the polycrystalline FeSi ribbon. The latter parabolic contribution arises if our estimate for the baseline of $\dot{u}$ for run i still contains a small error, see the discussion after Eq. (B1). The unfolding shown in the main text in Fig. 3(a) has been done using $\tau = 0.055$. In our chosen units, $w = 1$ corresponds to 50 ms $\sim$ 1.385 μm. The number of domain walls is estimated to be around 5.

Appendix G: Velocity correlations $\hat{\Delta}_{\dot{u}}(w)$

Measurements of the velocity correlations $\hat{\Delta}_{\dot{u}}(w)$ for our samples are shown in Fig. 10. The scale on which $\hat{\Delta}_{\dot{u}}(w)$ decays to zero is the same as the correlation length ρ of $\hat{\Delta}(w)$ defined in Eq. (C1).

CONTENTS

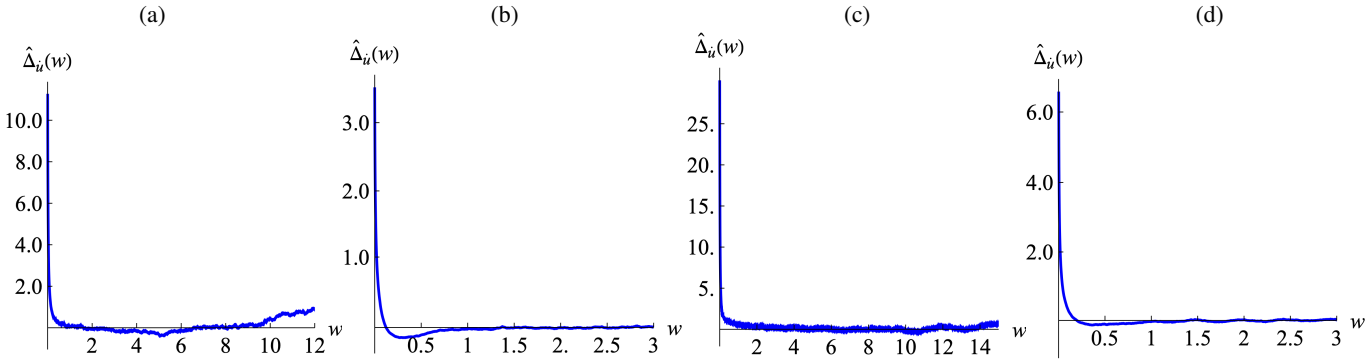

FIG. 10. The correlation function $\hat{\Delta}_{\dot{u}}(w)$ of the domain wall velocity $\dot{u}$. The scale on which $\hat{\Delta}_{\dot{u}}(w)$ decays to 0 is the correlation length ρ of $\hat{\Delta}(w)$. Plots are ordered, as in the main text, for (**a**) FeSiB film (SR elasticity, no eddy currents). (**b**) FeCoB ribbon (SR elasticity, eddy currents). (**c**) NiFe film (LR elasticity, no eddy currents). (**d**) FeSi ribbon (LR elasticity, eddy currents).